New challenges in experimental unsaturated soil mechanics. Experimental upscaling of an engineered gas-permeable seal

Enrique Romero[1,2*], *Clara* Alvarado[1], and *Antonio* Lloret[2]

[1]International Centre for Numerical Methods in Engineering (CIMNE), Barcelona, Spain
[2]Universitat Politècnica de Catalunya (UPC), Barcelona, Spain

Abstract. An example of upscaling phenomena with experimental techniques is presented and discussed within an engineered seal concept for a future deep geological repository for low and intermediate radioactive waste mainly produced by the energy/medicine/industry sectors. The seal will undergo a long-term saturation stage and subsequent gas transport through such a barrier. Consequently, gas entrapment and generation processes (dominated by the degradation of organic substances and metals) are expected to occur in the emplacement caverns along the pollutant waste storage. The case concerns a compacted 80/20 (dry mass) sand/bentonite S/B mixture with a complex microstructure that significantly evolves on hydration affecting the gas transport properties. This type of seal limits the gas pressure by increasing its gas transport capacity (gas-permeable seal). The large-scale and demonstration experiment GAST (Nagra's GTS, Switzerland) focuses on the S/B response to saturation and the gas transport capacity in the later gas invasion phase. A series of laboratory experiments running parallel to the *in situ* test and bridging different scales (from bentonite inter-sand filling microstructural tests and point tests to dm-scale mock-ups) are discussed within the saturation, gas breakthrough pressure and gas dissipation process of the gas-permeable seal context.

1 Introduction

Advanced experimental tools to approach phenomena at different scales for observing and interpreting multiphase (liquid, gas and solid) motion in porous materials and physical larger-scale mock-ups to support, demonstrate and mimic field tests are required to expand our capability to predict the response of unsaturated porous media in real-life engineering applications and emerging technologies [1]. Within this context, experimental techniques should not be merely understood as standard tools for model validation and parameter estimation in model calibration runs.

The current contribution focuses on recent tests at the Geotechnical Laboratory of the Universitat Politècnica de Catalunya (Spain). Different phenomena dealing with unsaturated soils have been approached at varying observation scales (from pore/grain level, point tests, and mock-up experiments to progressively upscale to the application). The studied case concerns storage with an engineered seal for a future deep geological repository for low and intermediate-level waste mainly produced by the energy sector. Gas entrapment and generation processes (dominated by the degradation of organic substances and metal deterioration by corrosion) are expected to occur after a long-term saturation.

Conventionally, two ways of gas dissipation have been considered. By allowing it to slowly diffuse through the pore water in a saturated bentonite mixture with a high gas breakthrough pressure. Alternatively, in the case described here, letting the gas pass using the concept of a gas-permeable seal. This concept was developed in the Swiss sectoral plan process for deep geological repositories to increase the backfilled structures' gas transport capacity without compromising the engineered barrier system's retention capacity and low water permeability. The design option is called an 'engineered gas transport system' EGTS [2] and involves a specially designed and compacted sand/bentonite S/B sealing mixture.

A large-scale 'GAs permeable Seal Test' GAST launched in 2011 at Nagra's Grimsel Test Site GTS (Nagra stands for 'National Cooperative for the Disposal of Radioactive Waste', Switzerland) is currently running to demonstrate the effective functioning of this EGTS concept during gas transport after long-term saturation with representative boundary conditions [3]. The test uses a dynamically compacted S/B mixture in different layers with low bentonite content (20% in dry mass). In addition, a supporting laboratory program at different scales was initiated in 2019 involving microstructural tests, point tests and mini-GAST mock-up experiments at dm-scale. The multi-scale program aims at helping interpret pore-scale phenomena, upscaling the hydromechanical and gas performance of the S/B system and providing a bridge between the well-investigated performance at dm-scale and the full-scale test at GTS. In addition, the mock-up

* Corresponding author: enrique.romero-morales@upc.edu

laboratory experiments were also aimed at demonstrating the EGTS functioning under different controlled scenarios (different stress states, gas injection pressures, volume or pressure rates for gas injection, and detecting self-sealing effects after the first gas breakthrough event). To this aim, mini-GAST mock-ups should mimic as close as possible the GAST test. Consequently, the design should allow for a dynamically compacted and layered S/B, and water and gas should flow parallel to compaction layers.

2 The *in situ* demonstration test and dm-scale mock-ups developed

As previously indicated, the full-scale and fully-instrumented GAST, emplaced in a tunnel in granitic rock at the GTS, aims to demonstrate the EGTS concept's effective functioning (to release gas pressure) at a realistic scale with representative boundary conditions and up-scaled gas/water permeabilities to perform reliable long-term predictions of the seal behaviour [3, 4]. The seal consists of 23 horizontal layers (100 mm in height) of compacted S/B with a length of 8.0 m and a total height of 2.3 m. The S/B is surrounded by MX-80 type granular bentonite GB to avoid water or gas by-pass. Vertical granular filters on both ends are used for initial hydration and later gas injections. The S/B is dynamically compacted at an average water content 10-11% and dry density 1.65-1.73 Mg/m^3. GB is emplaced at a mean water content of 10% and dry density 1.45-1.50 Mg/m^3. Figure 1 shows the GAST's schematics (cross-section and 3D view) with the different components (a compacted core of S/B in lifts surrounded by GB) and their dimensions.

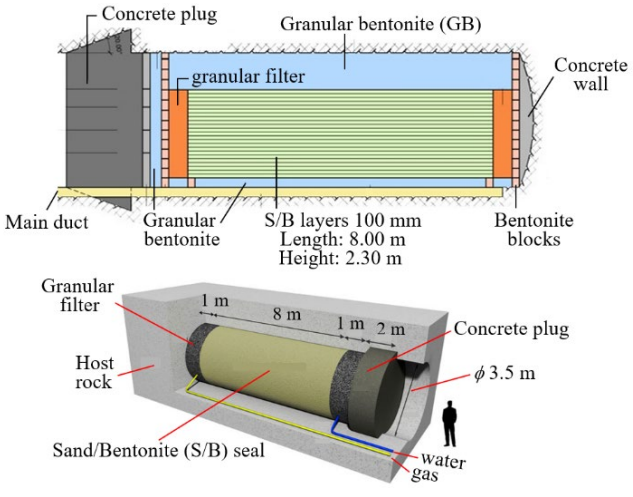

Fig. 1. Schematics of the *in situ* constant volume GAST experiment showing the compaction layers of the S/B core, the surrounding GB and the granular filters on both ends for gas/water injections. Adapted from [4].

A gas pre-test was performed in 2018 that demonstrated significant properties of the EGTS, including the transport of gas into the barrier at low gas-entry pressures and the low water permeability on re-saturation. During this pre-test, a channel-like gas transport pathway was formed close to the S/B and GB interface at the top (Figure 1). Subsequently to the gas pre-test, the pressurisation and homogenisation of liquid pressure proceeded until a target pressure in the filter elements close to 2 MPa was reached and kept constant.

Based on the enhanced understanding derived from the pre-test, an updated experimental program was designed that comprised dedicated characterisation tests of the S/B at different scales and the development of two dm-scale mock-ups mimicking the *in situ* test. Within this last context, mini-GAST mock-ups allow for a dynamically compacted and layered S/B and water and gas flowing parallel to compaction layers. They also mitigate any by-pass flow through the S/B and GB interface, and a pressure/displacement control mobile lid is envisaged to apply the vertical stress or the constant volume condition while inducing the liquid pressurisation to avoid any 'hydraulic fracturing' (water by-pass). In addition, the mobile lid allows a 'Skempton B-check' after saturation (inducing a change in total normal stress and recording water pressure change under undrained conditions). Furthermore, lateral cylindrical sintered stainless steel filters speed up the saturation process besides filters at both ends. Therefore, two mock-up prototypes were developed: 1) a mid-scale mock-up prototype MU-B (200 mm in length and 100 mm in diameter with three controlled compaction lifts with sub-layering and five lateral filters) to improve know-how, followed by 2) a larger-size mock-up prototype MU-A (500 mm in length and 300 mm in diameter with three layers and three controlled sub-layers each, and ten lateral filters). The prototypes are highly instrumented with local total stress sensors, pore pressure transducers, pressure/volume controllers at the inlet/outlet and lateral filters, gas mass/volume flowmeters, thermocouples, and LVDTs. In addition, the MU-B mock-up includes three load cells to monitor the normal stress applied to the compacted layers.

Using a metallic kneading roller, a 7-mm layer of GB (passing ASTM #40) was installed in MU-B at water content above the plastic limit. Next, the S/B core was prepared in three 28-mm layers by dynamic compaction at standard Proctor energy of 600 kJ/m^3. The samples were prepared under high relative humidity to preserve their initial water content.

Figure 2 at the top shows the U-shaped body of the MU-B prototype with the installed GB layer and the dynamically compacted S/B layers. In the middle of the figure, the two working positions of the mock-up are indicated. First, saturation is envisaged in the vertical working position with a vertical flow of demineralised water parallel to compaction planes with air released at the top. Then, nitrogen injection is performed with a horizontal flow parallel to compaction layers (horizontal working position). The bottom of the figure shows cross-sections with the instrumentation. Figure 3 presents photographs of MU-B in the vertical working position during saturation and in the horizontal position during N_2 injection with pressure/volume controllers, the instrumentation and the data acquisition system.

The mock-up results allowed the interpretation of the loading/saturation process (total stress relaxation at

constant volume and swelling pressure evolution), the water permeability with flow parallel to compaction planes, the effect of the stress state on the gas breakthrough pressure, the detection of some increase of total stress just before the gas breakthrough at constant volume, the gas effective permeability after breakthrough, as well as the snap-off pressure difference that blocks advective gas transport through the S/B.

3 Materials used in the research and initial state

The EGTS concept, using appropriate S/B mixtures, provides increased gas transport capacity of the backfilled underground structures without significantly impacting their water permeability and retention functions [2-4]. In addition, the *in situ* Gas Migration Test in Engineered Barrier System GMT (1997-2002), performed at Nagra's GTS, in which a Sand/Kunigel VI Bentonite mixture (80/20 in dry mass) was successfully used [5, 6], indicated the adequate proportion of bentonite considered in the GAST. So, the S/B mixture's constituents were Strobel quartz sand BS650 and granular MX-80 type bentonite in the proportion above.

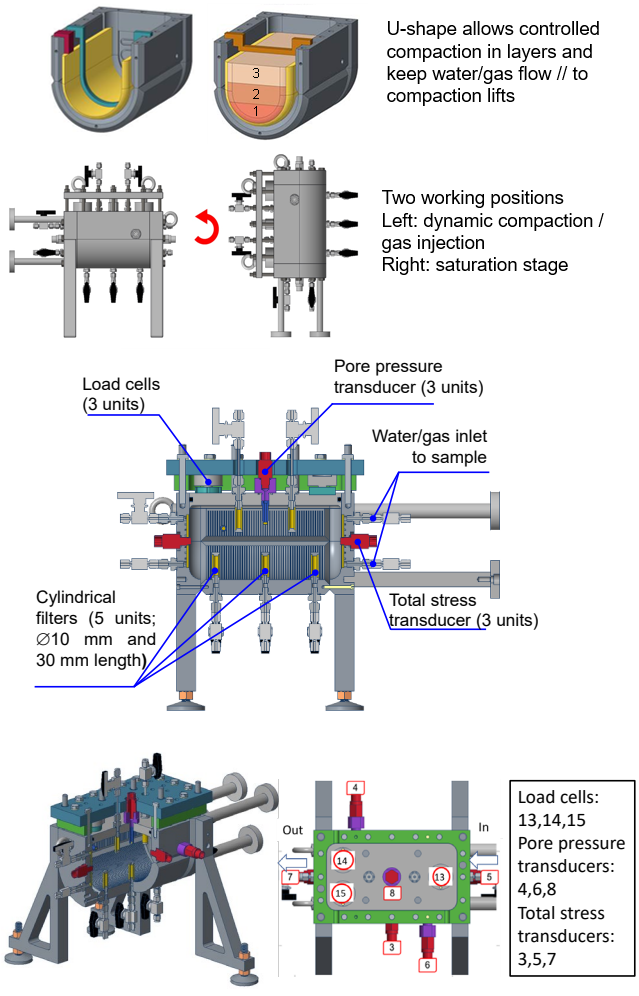

Fig. 2. Top: U-shaped body with compacted S/B layers and the two working positions. Bottom: Cross-sections of constant volume mock-up MU-B (200 mm in length and 100 mm in diameter) with instrumentation [7].

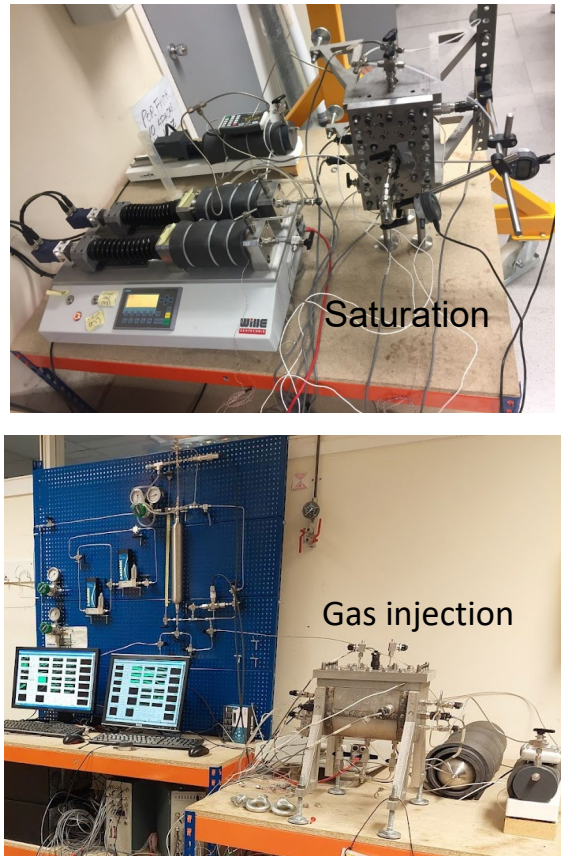

Fig. 3. Photographs of mock-up MU-B during saturation (top) and gas injection (bottom) with pressure/volume controllers, instrumentation and data acquisition system [7].

MX-80 type GB is an aggregated structure initially formed by particles of considerable size (up to 7 mm). The geotechnical properties of the constituents (GB and sand) and the mixture (S/B) are summarised in Table 1. Other properties can be found in [8, 9].

Figure 4 shows their initial grain size distributions. During compaction, the larger bentonite aggregates are crushed.

Table 1. Constituents and mixture geotechnical properties.

Properties	GB MX-80 type	Strobel SiO_2 sand BS650	S/B (80/20)
Density of solids (Mg/m^3)	2.74	2.65	2.67
Plastic limit (%)	65	-	-
Liquid limit (%)	440	-	-
Specific surface area (m^2/g)	590	0.0046	118
Maximum grain size (mm)	7.0 (initial)	0.71	-
Mean grain size (mm)	2.3 (initial)	0.52	-
Hygroscopic water content (RH = 40%) (%)	6.51	-	1.30

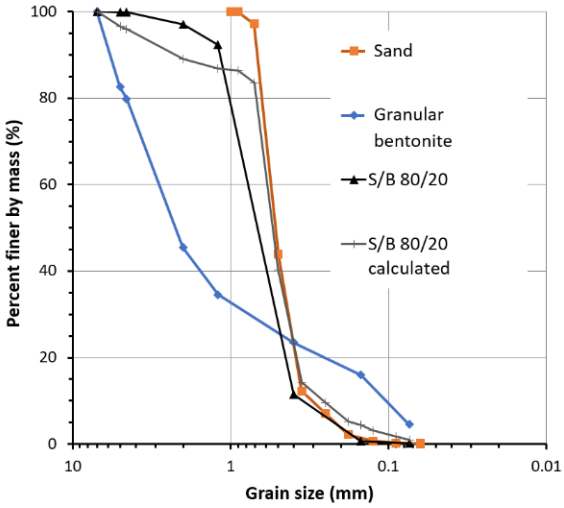

Fig. 4. Grain size distribution curves of the materials.

Dynamic Proctor compaction tests were performed in oedometer (50 mm in diameter) and conventional Proctor (102 mm in diameter) moulds at different compaction energies (per unit volume of soil) and mean water content 11.4% (equivalent to the one used in GAST). Figure 5 summarises the maximum dry densities at various energies. In addition, mean values of dry densities in MU-B and GAST are indicated for reference. These dry densities (around 1.65 Mg/m^3) have been selected to ensure a swelling pressure > 200 kPa, which is higher than the air-entry value of the S/B mixture (between 157 kPa and 189 kPa [5, 6]).

The initial state of the different materials installed in MU-B is summarised in Table 2. Matric suction was measured with a miniature T5x tensiometer/INFIELD7 readout unit.

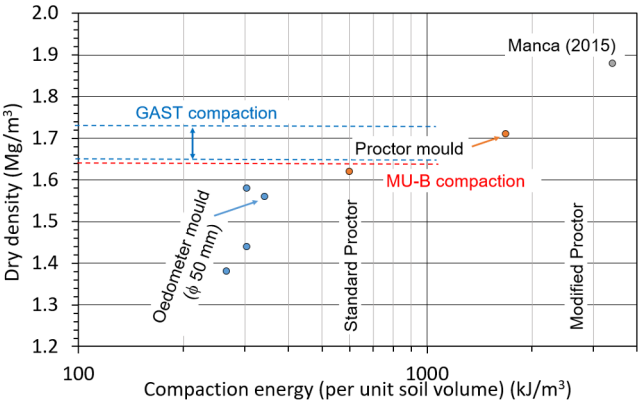

Fig. 5. Dynamic compaction of S/B at different energies (per unit soil volume) and water content of 11.4 %. Dry densities in GAST and MU-B. Compaction at high energy [9].

4 Experimental results at different testing scales

4.1 Microstructural studies and relationship with gas dissipation tests

Gases in a saturated S/B mixture will be initially dissolved in the porewater, and eventually, when the solubility limit is exceeded, a separate phase may form (two-phase flow) when the gas-entry value is reached, affecting the deformation of the medium. Consequently, gas transport properties are controlled by both hydraulic and mechanical properties and the state of the material (initial state and the stress paths followed). Within this context, microstructural features (as-compacted and their evolution) are essential since they affect the connectivity of pores and the local variability of porosity.

Table 2. S/B and GB's initial state installed in MU-B.

Variable	S/B	GB (passing ASTM #40)
Mean dry density (Mg/m^3)	1.64±0.01	0.85±0.01
Mean water content (%)	12.2±0.4	80.7±0.2
Void ratio (-)	0.63±0.02	2.21±0.01
Degree of saturation (%)	52±2	100
Matric suction (kPa)	around 200	100 to 200
Maximum compaction stress (MPa)	between 0.8 and 1.0	-

Figure 6 shows ESEM photomicrographs at different hydraulic states (as-compacted and saturated) of the S/B of GMT with the same bentonite proportion and at a lower void ratio between e=0.425 and 0.472 obtained by [5, 6, 10]. A complete filling of the inter-sand space with low-density bentonite is observed in the saturated mixture. Mercury intrusion porosimetry data reported by [5, 6, 10] were also used to estimate the degree of bentonite filling (volume of bentonite divided by total pore volume), which will be used later to assess gas transport properties at different hydraulic states.

Hokari *et al.* (1996) [11] suggested mechanisms for gas penetration in voids filled with low-density bentonite in 85/15 S/B compacted at a dry density of 1.8 Mg/m^3. Figure 7 presents an updated version of one of their figures to summarise significant aspects during gas penetration and the anticipated dry density of the bentonite after filling the inter-grain porosity (around 0.65 Mg/m^3). At the gas-bentonite interface, some bentonite material is also expected to consolidate, and some drying may occur once flow paths are developed. Swelling pressure has been measured for GB (passing ASTM #40) at a dry density of 0.85 Mg/m^3 resulting in a value close to 200 kPa.

Tests have been performed in S/B to determine the effective gas permeability, a measure of the ability of gas to flow in the presence of a water phase (product of the relative permeability and the intrinsic permeability). Tests at degrees of saturation below 90% have been reported by [6, 10] on GMT S/B (void ratios between e=0.40 and 0.60). Additional tests incorporate gas dissipation results in MU-B after gas breakthrough in initially saturated S/B. Test results are fitted to a modified Kozeny-Carman equation, as proposed by [10]. The following expressions for the effective gas

permeability incorporate changes in the degree of saturation S_r and the macrovoid ratio e_M:

$$\frac{e_M}{e} = 1 - (\alpha + \beta S_r)\ ;\ \alpha + \beta S_r \leq 1$$
$$K_{eff} = \left[1 - \left(\frac{S_r - \alpha}{1 - \alpha}\right)^3\right]\left[A\frac{e_M^3}{1 + e_M}\right] \quad (1)$$

where $e_M = e - e_m$ (e_m is the microvoid ratio inside intra-aggregate pores in GB, and e = 0.63 has been considered to represent MU-B results according to Table 2). Moreover, α and β are microstructural parameters accounting for the expansion of the intra-aggregate pores with the degree of saturation. The Grant model for relative gas permeability in Equation (1) enhances gas mobility (fewer interactions between phases).

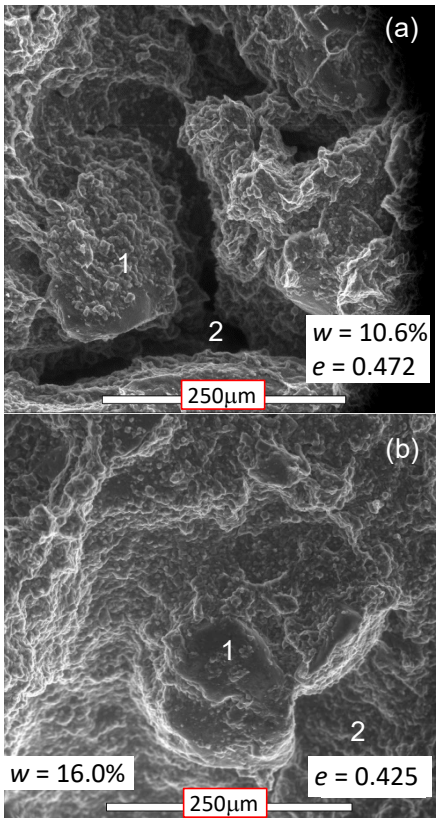

Fig. 6. ESEM photomicrographs on GMT S/B at different hydraulic states. a) As-compacted state (degree of bentonite filling around 70%). b) After saturation with a full degree of bentonite filling (adapted from [5, 6, 10]).

Different test results are summarised in Figure 8, and the fitted curve (data are described in the legend). Fitted parameters are presented in Table 3. Intrinsic water permeability results are also plotted in the figure, based on [10] and MU-B results obtained with flow parallel to compaction layers and the infiltration column.

Figure 9 summarises effective gas permeability versus the inter-sand skeleton's bentonite filling percentage. The figure includes results by [10] on GMT S/B, in which the bentonite filling percentage at different hydraulic states was estimated based on mercury intrusion porosimetry results. The figure also plots new data based on gas dissipation tests obtained in MU-B after gas breakthrough events. Close to full saturation, powder filling the inter-sand volume is assumed F=100%. The figure shows a good agreement between the different results despite being prepared at various void ratios. Further research should include the void ratio and the connectivity of the porous network.

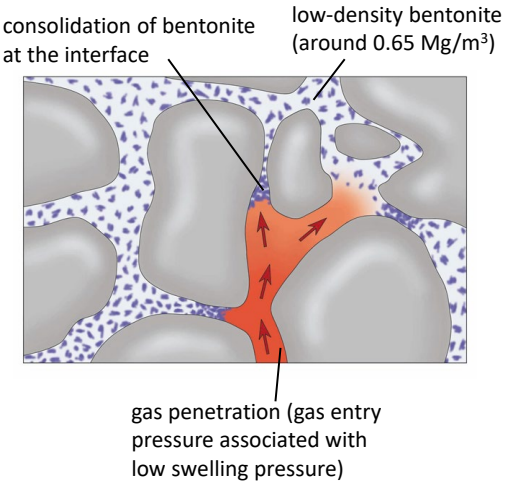

Fig. 7. Gas transport mechanisms in S/B (adapted from [11]).

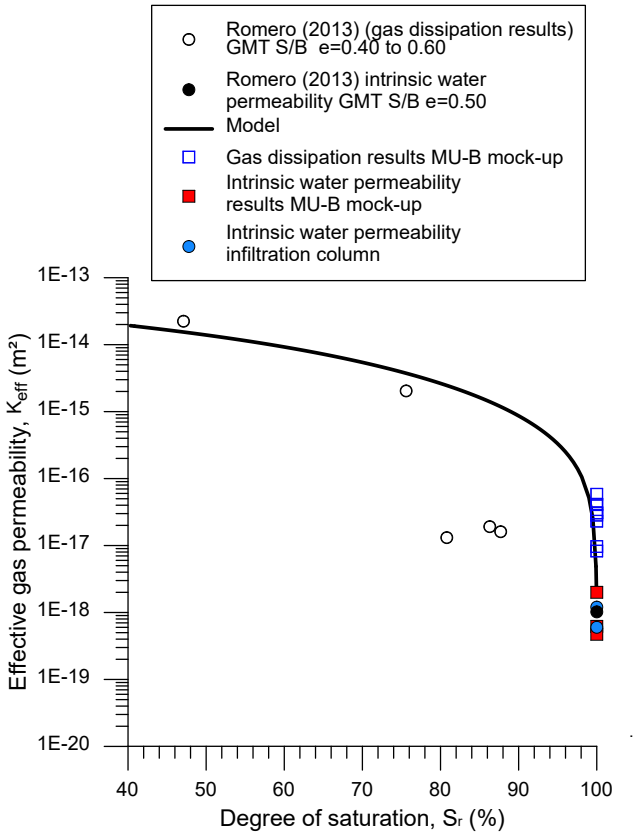

Fig. 8. Effective gas permeability at different degrees of saturation [6, 10], including gas dissipation data in MU-B after gas breakthrough. Intrinsic water permeability results in MU-B with flow parallel to compaction layers. Intrinsic water permeability values in the infiltration column.

Table 3. Fitted parameters (Equation (1)).

Parameters	Value
α	0.28
β	0.53
A	81×10^{-14} m^2

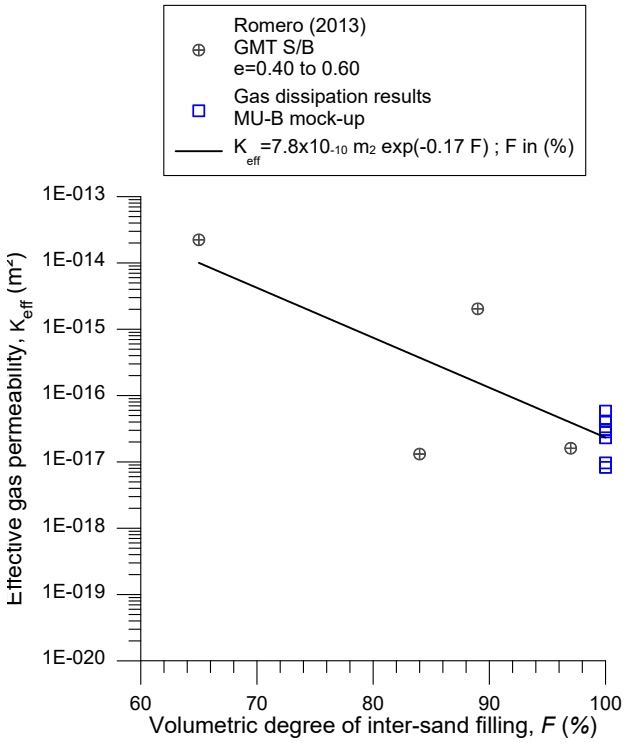

Fig. 9. Effective gas permeability *versus* degree of bentonite filling. Results on GMT S/B during wetting [6, 10]. Gas dissipation results on MU-B after gas breakthrough events.

4.2 Point and mid-scale tests: oedometer, water retention and infiltration column tests

Three conventional oedometer tests were carried out on S/B samples of 50 mm diameter and 10 mm initial height. The initial water contents of the three samples were 3.49%, 12.19% and 11.88%, and the initial dry densities 1.61, 1.58 and 1.69 Mg/m^3, respectively. The stress paths involved loading to 50 kPa (unsaturated state), soaking under constant stress, drained loading under full saturation conditions in steps until 800 kPa and then drained unloading.

Figure 10 shows the evolution of the void ratio in these three tests. Expansions were observed at 50 kPa on soaking in all the samples. Yield stress under saturated conditions of around 200 kPa can be estimated in test OE1 (at an initial dry density of 1.61 Mg/m^3). This value is consistent with the measured swelling pressure of 200 kPa under constant volume conditions, starting at an initial dry density of 1.61 Mg/m³ and water content of 11.58%.

High compressibility on drained unloading under saturated conditions was observed in the three samples. The time evolution of vertical displacement during consolidation has been interpreted using a non-linear curve-fitting algorithm to determine the different conventional parameters used in consolidation analysis following Terzaghi's theory. The fitted parameters allow for obtaining the saturated water permeability results, plotted in Figure 11. These fitted values are compared to water permeability data obtained with controlled-gradient tests in MU-B with flow parallel to compaction layers. Only the result of the first test in MU-B appears a bit high, which may have been affected by an initial flow of water due to low normal stress that induced a minor internal erosion of bentonite particles. However, generally speaking, a good consistency is detected between the different results.

To obtain the water retention curve of the S/B, matric suction values were measured with a miniature tensiometer (T5x tensiometer/INFIELD7 readout unit) after dynamic compaction and post-mortem infiltration tests. These results are presented in Figure 12 and correspond to wetting paths. In addition, a controlled-suction drying under oedometer conditions and low net vertical stress is shown, based on data reported by [5, 10] on GMT S/B bentonite mixture (void ratio between 0.503 and 0.489). Finally, the extreme values of first gas breakthrough pressures (excess of gas over water pressure) obtained in the MU-B are also plotted (between 130 kPa and 220 kPa), showing a good consistency with the air-entry value of the S/B (on drying and corresponding to degrees of saturation in the range 93% to 96%). Additional values of this drying curve are summarised in Table 9.

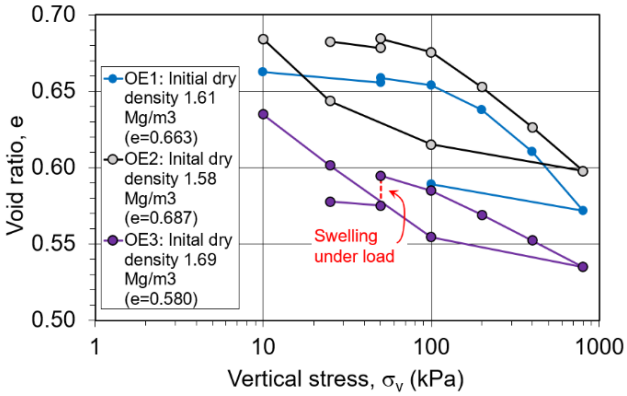

Fig. 10. Void ratio changes on loading and soaking under oedometer conditions (refer to the text for the stress paths followed).

Water retention curves (s is the matric suction) along the wetting paths were fitted to the following expressions that consider the effects of porosity n on van Genuchten parameters $\lambda(n)$ and $P(n)$ [12]:

$$\frac{S_r - S_{r\,res}}{1 - S_{r\,res}} = \left[1 + \left(\frac{s}{P(n)}\right)^{\frac{1}{1-\lambda(n)}}\right]^{-\lambda(n)} \qquad (2)$$

$$P(n) = P_0 e^{a(n_o - n)} \;;\; \lambda(n) = \lambda_0 e^{b(n_o - n)}$$

The effects of the increase of $P(n)$ with the reduction of porosity are observed in the interpolated curves. A similar dependence on porosity can be used for the drying curves. Table 4 summarises the fitted parameters. As observed, the residual degree of saturation is also close to the value α=0.28 reported in Table 3.

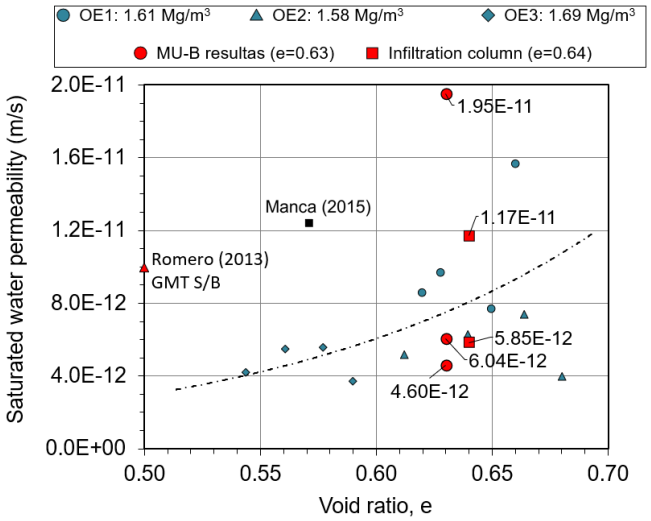

Fig. 11. Saturated water permeability as a function of void ratio. Back-analyses of one-dimensional compression test results. Controlled-gradient tests in MU-B with flow parallel to compaction layers. Infiltration column results and data reported by [5, 6, 10] and [9].

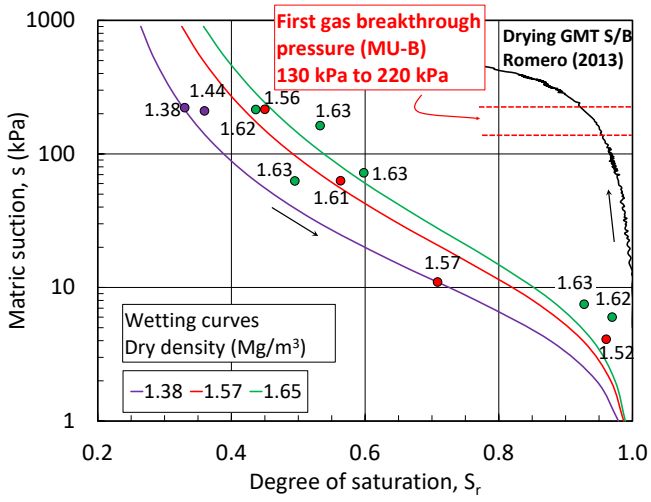

Fig. 12. Water retention curves on wetting of S/B mixture for different dry densities. Water retention curve on drying GMT S/B using a controlled-suction technique [5, 10]. Values of first gas breakthrough pressures in MU-B.

Two water infiltration column tests were performed for 22 and 168 days. The S/B was dynamically compacted in 4 layers inside a cylindrical PERSPEX® mould of 70 mm in diameter and 160 mm high. The initial water content of the soil was (11.8±0.1)%, and the dry density (1.63±0.01) Mg/m^3. The results are shown in Figures 13 and 14 regarding the time evolution of the infiltrated cumulative water volume and saturation profiles, respectively. In addition, two predictions were plotted in the figures using a simplified and uncoupled 1D axisymmetric one-phase flow model (CODE_BRIGHT [12]). As observed in Figure 13, simulation A fits better the final evolution of the cumulative water volume, while simulation B matches better the initial trend.

The back-analysed parameters of the retention curve and water permeability (intrinsic permeability K and relative permeability) and the initial conditions (subscript 'ini') are summarised in Table 5. The expression of the water retention curve is equivalent to the one indicated in Equation (2) with constant van Genuchten's parameters λ and P. The expression of the relative water permeability is $k_{rw} = S_r^{\gamma}$. The fitted parameters are consistent with the previous results. For example, refer to Figure 8 for the intrinsic water permeability values and Table 4 for van Genuchten's parameters. In addition, the exponent back-analysed in the relative water permeability is also consistent with the exponent used in the high gas mobility Grant expression for relative air permeability of Equation (1).

Table 4. Fitted parameters (Equation (2)).

Parameters	Value
$S_{r\,res}$	0.20
P_0	7.5 kPa
a	5.00
λ_0	0.28
b	-2.37
n_0	0.41

Table 5. Model parameters and initial conditions used in the two simulations of infiltration column tests (A and B).

Case	A)	B)
Sr_{min}	0.20	0.20
λ	0.40	0.40
P (MPa)	0.020	0.018
K (m^2)	6.0E-19	1.2E-18
γ	2.7	3.0
s_{ini} (MPa)	0.087	0.078
S_{rini}	0.491	0.491
n_{ini}	0.391	0.391

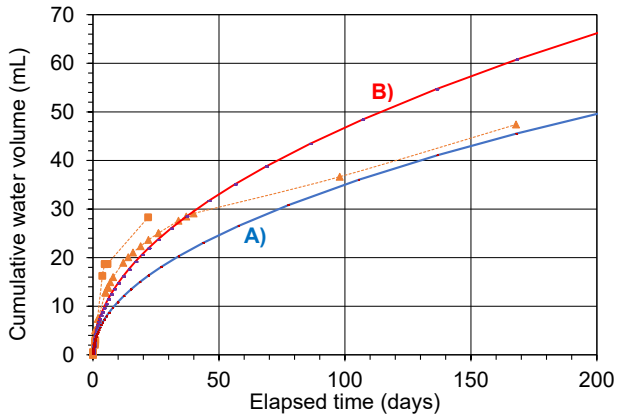

Fig. 13. Measured (dashed lines) and modelled (solid lines A and B) infiltrated water volume in column tests.

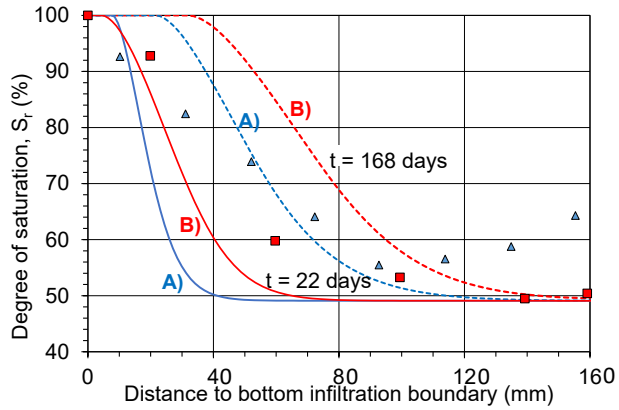

Fig. 14. Measured and modelled (dashed/solid lines A and B) profiles of the degree of saturation for two infiltration times in column tests.

4.3 Mini-GAST mock-up tests (dm-scale tests)

This section reports selected results performed with MU-B. A summary of the different stages followed is indicated in Table 6, which involved 204 days for the first test and 374 days for the second one. The results allowed analysing loading under as-compacted conditions (total stress relaxation at constant volume) and the saturation processes (total stress evolutions, water permeability), the effect of the stress state on repeated processes of gas breakthrough pressure (including two re-saturation stages), the effective gas permeability values after breakthrough events, as well as the snap-off pressure difference (gas pressure above water pressure) that blocks advective gas transport through the S/B.

After S/B compaction in a humid environment, the top mobile lid is placed. The displacement-controlled mobile lid allows applying initial normal stress (close to the compaction stress, i.e., between 0.8 MPa and 1.0 MPa, as indicated in Table 2) to avoid technological gaps. Figure 15 shows the initial increase of normal stress after compaction (average normal stress from load cell readings 13, 14 and 15 in the schematic of the figure) and its relaxation with time at constant volume to reach a residual value of around 285 kPa. The figure also includes the evolution of horizontal stresses measured by the local total stress sensors (numbers 3 at the U-shaped body, and 5 and 7 at the inlet and outlet, respectively). As a result, the coefficient of lateral stress at rest K_0 of the S/B varies between 0.56 and 0.70.

Table 6. Typical testing stages carried out in MU-B (1st and 2nd tests).

Stages	Description
A	Sample compaction and stress relaxation
B	Saturation of the material. Water pressurisation. Determination of water permeability
C	1st gas injection. Gas breakthrough pressure and effective gas permeability after breakthrough
D	Re-saturation and water pressure equalisation. Determination of water permeability
E, F	2nd gas and 3rd gas injections. Effective gas permeability after breakthrough
G	Re-saturation and water pressure equalisation. Determination of water permeability
H, I	4th gas injection and 5th gas injections. Effective gas permeability after breakthrough
J	Dismantling of mock-up/post-mortem tests

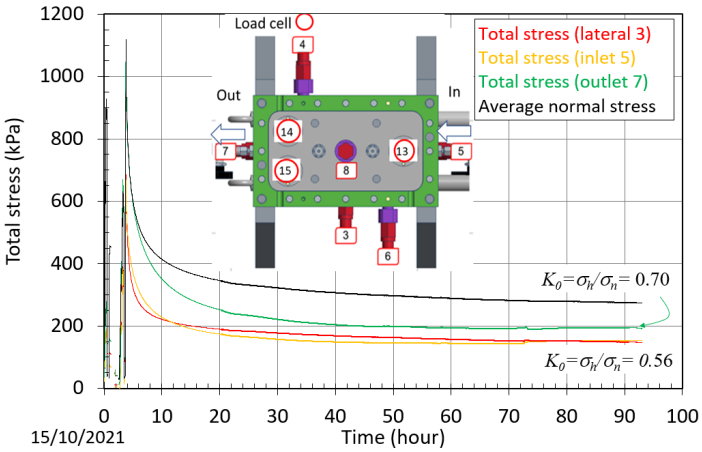

Fig. 15. Normal stress increase during displacement-controlled compression and stress relaxation under a constant volume of S/B before the saturation stage of MU-B. Evolution of total stress readings at different positions.

The cell is vertically positioned during water injection to release air through the top outflow filter better. A slow pressure-controlled water injection (distilled water) is applied at the base and cylindrical lateral filters (pressure rate < 0.1 kPa/min with equalisation steps at constant inlet pressure), leaving the top outlet filter at low pressure (5 kPa). Continuous verification of the average normal stress and local total stress sensors ensures local net stresses are lower than the saturated preconsolidation stress to avoid any local collapse on wetting (activation of the loading-collapse yield locus [13]). The saturated preconsolidation stress is around 200 kPa, similar to the one shown in Figure 10 for test OE1 at an initial dry density of 1.61 Mg/m^3, and close to the expected swelling pressure. In addition, this continuous verification ensures avoiding the localised

passage of water throughout low-stressed zones. Figure 16 presents the time evolution of the average normal stress and three local total stress sensors (numbers 3, 5 and 7 at the U-shaped body, the base and the top, respectively) throughout 113 days (80 days with lateral filters open and 33 days with lateral filters closed). The average normal stress reached 340 kPa, and local total stresses at points 3 and 5 stabilised at values close to 300 kPa, while the total stress at 7 was 230 kPa (water pressure at the inlet 150 kPa and 5 kPa at the outlet with lateral filters closed). The average effective stresses were between 220 kPa and 260 kPa under steady-state water flow conditions. Figure 17 summarises the evolution of inlet and outlet pressures and local pore pressure transducers (numbers 4, 6 and 8 in the figure) during water pressure increase and saturation (maximum water pressure at the inlet of 150 kPa and outlet pressure kept at 5 kPa). Afterwards, the lateral inlet filters are closed, and the boundary pressure conditions are kept for 33 days to reach steady-state conditions to measure water permeability parallel to compaction layers. The measured saturated water permeability reached a value of 6.0×10^{-12} m/s, slightly below the value measured in the first MU-B test (1.9×10^{-11} m/s in stage B). The difference could arise due to the initial water flow in the first MU-B test at low normal stress that induced a minor internal erosion of bentonite particles. The following section compares these results to other test data (Table 9).

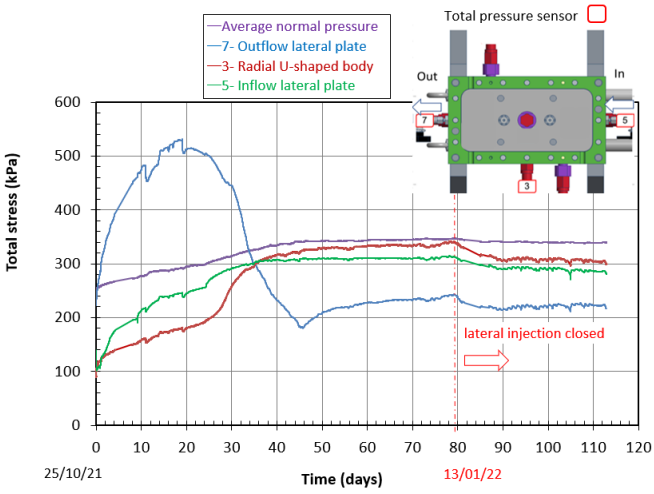

Fig. 16. Normal stress and local total stress changes during the saturation stage B (refer to Table 6).

The top valve is closed at the end of stage B to record the transient pressure increase towards a homogeneous back-pressure of 450 kPa. Next, the mobile lid is activated to allow for a 'Skempton B-check' under undrained conditions and increase the pore pressure to 2.3 MPa by mechanical actions. Figure 18 shows the evolutions of the increments in total normal stress and local pore pressures (numbers 4, 6 and 8 in the figure) tending to high values of the *B* parameter (close to 1).

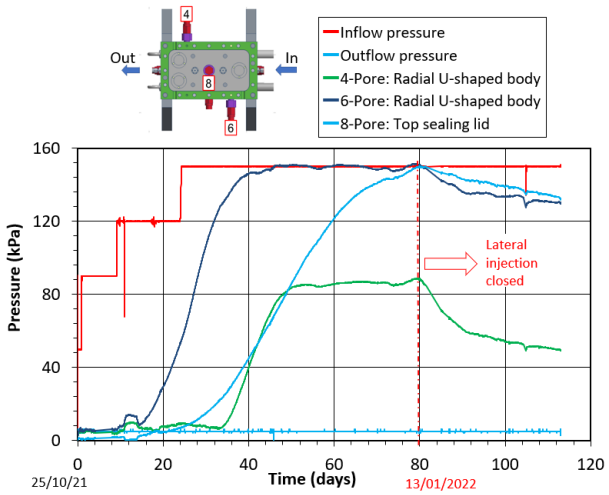

Fig. 17. Time evolutions of inflow and outflow pressures and local pore pressure transducers during water pressure increase and saturation (stage B, Table 6).

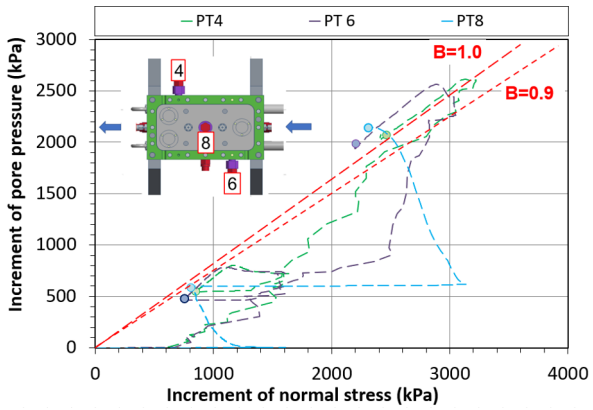

Fig. 18. Time evolution of increments of normal stress and local pore pressures (numbers 4, 6 and 8 in the schematic) during undrained loading (stage B, Table 6). Skempton B parameter close to 1.

Afterwards, the cell is horizontally oriented for the different gas injection stages. A slow pressure controlled N_2 gas injection (rate < 0.08 kPa/min) is applied on one end until the breakthrough is reached. During the subsequent gas flow, the effective gas permeability is measured. No significant differences were observed in water permeability values measured after gas breakthrough and re-saturation processes in the second MU-B test (6.0×10^{-12} m/s in stage B and 4.6×10^{-12} m/s in stage D, Table 6). These values are consistent with the ones obtained in other laboratory tests (refer to Figure 11).

Figure 19 shows the first breakthrough process in the second MU-B test. An N_2 inflow pressure of 2320 kPa was applied, whereas a water pressure of 2100 kPa was kept in the outflow end. The breakthrough (with increased outflow volume) was observed six days after the start of the gas injection. Some increase in the total normal stress was also observed just before the gas

breakthrough at constant volume (from 2500 kPa to approximately 2520 kPa). This total normal stress increase could be related to preferential pathways' opening (dilation) along the compaction layers. Table 7 summarises the gas inflow and water outflow pressures measured throughout the other breakthroughs generated. Differences in pressures between 44 kPa and 220 kPa were measured. A decrease in breakthrough values could be observed as new gas injection events are induced without re-saturation. The breakthrough process generally develops at slightly excess gas pressure over water pressure (usually less than 190 kPa).

The inlet and outlet pressures generated after the breakthrough were allowed to equilibrate while keeping the inlet and outlet reservoirs at constant volume. A snap-off pressure that blocks advective gas transfer throughout the S/B was also detected. The first MU-B test registered values of the snap-off pressure differences between 36 and 53 kPa. Smaller values (about 0 to 3 kPa) were observed in the second test after various breakthrough and re-saturation cycles (refer to Table 7).

The effective gas permeability was evaluated after the breakthrough process considering the overall cross-section (gas permeability occurs along preferential local paths, and the reported values should be considered global). Table 8 presents the measured values of (global) effective gas permeability after the different breakthrough events. Values are usually higher than 1×10^{-17} m^2, except when re-saturation stages are performed, in which values below 1×10^{-17} m^2 have been measured, as observed in the table.

Figure 20 plots the effective gas permeability after breakthrough events at different average effective normal stresses (the two gas breakthrough tests with a previous re-saturation stage are also included). No clear dependence on the effective stress state is captured at the range of effective stresses plotted.

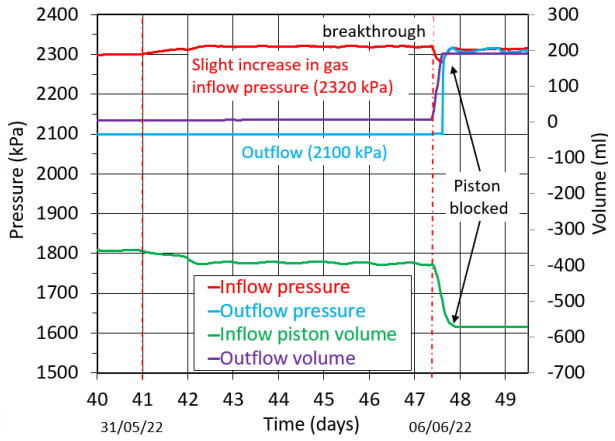

Fig. 19. 2nd MU-B test (stage C). First gas breakthrough event (with increasing outflow volume) at a pressure difference of 220 kPa (inflow gas pressure at 2320 kPa and outflow liquid pressure at 2100 kPa).

Table 7. MU-B first and second tests. Gas breakthrough and snap-off pressure differences.

Test-stage	Total normal stress (kPa)	Inflow gas (N_2) pressure (kPa)	Outflow pressure (kPa)	Difference in pressures† (kPa)
1-C	1280	1100-1080/*1038*	950/*1002*	150-130/*36*
1-E	1700	1550	1450	100
1-F	1700	1515/*1548*	1450/*1496*	65/*52*
1-H	1770	1569/*1603*	1501/*1550*	68/*53*
2-C	2500	2320	2100	220/*<30*
2-E$^+$	2668	2495	2315	180/*3*
2-F	2700	2377	2315	*62/1-3*
2-H$^+$	2907	2599/*2624*	2410/*2623*	189/*1*
2-I	2940	2660	2616	44/*1*
2-I	2925	2746/*2925*	2660/*2925*	86/*0*

(+) With a re-saturation stage before gas breakthrough
(†) Pressure difference at breakthrough event / *Snap-off pressure difference*

Table 8. First and second MU-B tests. Effective gas permeability values after breakthrough events.

Number of test and stage	Total normal stress (kPa)	Inflow pressure (kPa)	Outflow pressure (kPa)	K_{eff} (m^2)
1 – C	1280	1090-1080	950	4.14×10^{-17}
1 – F	1700	1515-1513	1450	4.08×10^{-17}
1 - H	1770	1603-1608	1501	2.84×10^{-17}
2 - C	2500	2320	2100	3.07×10^{-17}
*2 – E**	*2668*	*2495*	*2315*	*8.27×10^{-18}*
2 - F	2700	2376	2315	2.31×10^{-17}
*2 – H**	*2907*	*2599*	*2410*	*9.66×10^{-18}*
2 - I†	2940	2660	2616	5.83×10^{-17}

(*) *With a re-saturation stage before gas breakthrough*
(†) Outflow reservoir filled with N_2 gas

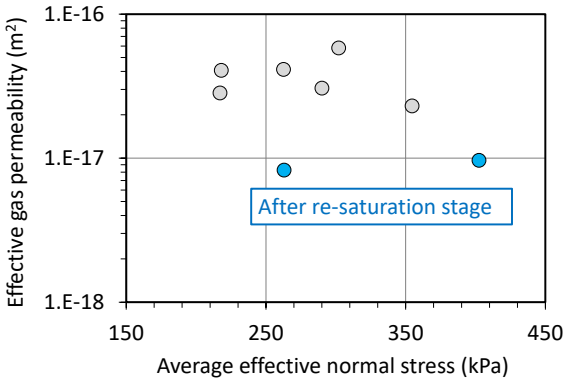

Fig. 20. Effective gas permeability after breakthrough events *versus* average effective normal stress (two gas breakthrough tests are included with a previous re-saturation stage that reported lower effective gas permeability values).

5 Discussions and concluding remarks

An example of upscaling phenomena with experimental techniques at different observation scales is presented and discussed related to the concept of a gas-permeable seal for a future deep geological repository for low and intermediate radioactive waste. This seal concept relies on an increased gas transport capacity without compromising its low water permeability.

The *in situ* GAST experiment used an S/B mixture (80/20 in mass) at a dry density between 1.65-1.73 Mg/m^3 to demonstrate large-scale and filter-to-filter gas flow in highly saturated S/B at stresses and pressure conditions comparable to those expected in the repository. However, due to the very long period required for saturation and its influence on the developed swelling pressure (affecting the confining stresses) and gas entrapment phenomenon, there is some concern that filter-to-filter gas transport cannot be fully demonstrated with this *in situ* test. Therefore, a decision was made to rescale this experiment to dm-scale mock-ups and replicate the processes followed under *in situ* conditions at equivalent stresses and pressures (compaction of layers, loading, saturation, water permeability measurement, gas injection, gas breakthrough, gas permeability measurement and re-saturation). Within this context, the new laboratory experiments that bridge different scales (small-scale laboratory tests and dm-scale mock-ups) will likely provide supporting evidence (saturation, gas breakthrough pressure, gas dissipation process) under well-controlled boundary conditions and initial state.

As discussed above, an important property is the adequate swelling pressure of the mixture (associated with the dry density of the S/B), which should be slightly higher (preferably slightly above 200 kPa) than the breakthrough pressure to avoid gas breakthrough phenomena at the interfaces. On the other hand, the saturated water permeability and the effective gas permeability are also essential in describing the properties of these seals. In general, the gas flow is expected to develop at a slight excess gas pressure over water pressure (usually less than 150 kPa). In addition, once developed, the effective gas permeability is also expected to be high (preferably greater than 1×10^{-17} m^2). On the other hand, the saturated water permeability should be lower than 3×10^{-11} m/s.

Nevertheless, the different phenomena' descriptions may differ depending on the observation scale (experimental observation). For example, suppose one refers to a gas entry in small-scale point or microstructural tests. In that case, one refers to the concept of gas-entry pressure on drying or water-entry on wetting, which is determined by the pore size, the connectivity of the pore network, the capillary phenomena (surface tension, wettability), and in the particular case of S/B to the dry density of the bentonite filling the inter-sand space. However, at dm-scale this phenomenon is referred to as breakthrough pressure (gas pathways generated following a saturation process) or snap-off pressures during gas dissipation (interruption of the advective gas transport). These concepts are more linked to interfaces (between materials or between compaction layers) and local spatial variability of porosity. In this context, the stress state is fundamental when describing these phenomena.

A similar discussion arises regarding the induced anisotropy of the mixture and the layering on compaction. The induced anisotropy, associated with a continuum approach, arises due to preferential vertical straining during 1-D compaction. This preparation technique affects the mechanical response (transversally isotropic fabric) and the two-phase flow response. Layering, a larger-scale concept involving compaction interfaces, has been a significant issue in the mock-up design (to mimic the expected field compaction in layers). This layered structure induces a structure with preferential paths for gas/water flow, which the stress field affects.

Regarding experimental results, water permeability values obtained by back-analyses of consolidation tests and column infiltration experiments are similar to the ones obtained by direct measurements in the mock-up tests. In addition, at the MU-B dm-scale, no significant flow increase was detected parallel to the compaction layers. Furthermore, water permeability values measured in MU-B after gas breakthrough and re-saturation processes are also similar (6.0×10^{-12} m/s after initial saturation and 4.6×10^{-12} m/s after gas flow). Nevertheless, a slightly higher value of 2.0×10^{-11} m/s was measured in the first MU-B test, which was affected by an initial flow of water due to low normal stress that induced a minor internal erosion of bentonite particles. Test results are summarised in Table 9, together with data obtained from point tests (PT in oedometer cells under controlled-gradient conditions) and the back-analysed transient flow of the infiltration column.

Pressure differences between N_2 and water ranging from 130 kPa to 220 kPa have been measured for the first gas breakthrough in the first and second MU-B tests. The lower values (between 130 kPa and 150 kPa) of the first MU-B test compared to the second MU-B (between 180 kPa and 220 kPa) could arise due to the initial flow of water at low normal stress that induced a minor internal erosion of bentonite particles. This pressure difference during gas breakthrough decreases after several cycles of breakthrough events without re-saturation until they reach values between 44 kPa and 86 kPa. Nevertheless, if re-saturation is allowed after the previous breakthrough event, higher values of pressure differences are recovered (between 180 kPa and 189 kPa). Test results are presented in Table 9, together with gas-entry values at different degrees of saturation obtained by [5, 10] on GMT S/B. Despite the different scales and phenomena involved, test results are consistent.

The gas flow measured after the breakthrough confirmed the high gas transport capacity of the S/B mixture. Relatively high values of (global) effective gas permeability were measured considering the overall-cross section of the MU-B (usually greater than 1×10^{-17} m^2). Effective gas permeability values below 1×10^{-17} m^2) were measured after a re-saturation stage of the previous breakthrough event. No clear dependence of the effective gas permeability on the average effective stress was captured at the range of effective stresses

considered. Test results are summarised in Table 9, in which point gas dissipation tests at different degrees of saturation obtained by [6, 10] on GMT S/B have been included. Gas flow continued after the breakthrough event under decreasing gas pressure difference between the constant volume inlet and outlet reservoirs. In addition, a small snap-off pressure difference that blocks advective gas flow was measured, and it decreases between 53 kPa and near 0 as the number of gas injection and re-saturation cycles increases.

A summary of selected properties of GB and S/B mixture according to different tests performed at the Geotechnical Laboratory UPC is presented in Table 9.

Table 9. Summary of selected properties of GB and S/B mixture according to different tests at varying scales performed at the Geotechnical Laboratory UPC.

Geotechnical property	**GB (passing #40 sieve) at 0.86 Mg/m^3**	**S/B at 1.64 Mg/m^3**
Swelling pressure on suction reduction at constant volume (kPa)	200 (PT)	100 (PT[1]) 200 (PT) 200 (MU-B)
Saturated water permeability (m/s)	2.5-5.7×10^{-12} (PT)	1.00×10^{-11} (PT[1]) 5.85×10^{-12} (IC) 1.17×10^{-11} (IC) 1.95×10^{-11} (*) 6.04×10^{-12} (+) 4.60×10^{-12} (++)
Effective gas permeability (m^2)	10^{-18} to 10^{-17} (PT)	1.91×10^{-17} (S_r=0.86) (PT[1]) 1.61×10^{-17} (S_r=0.88) (PT[1]) 4.14×10^{-17} (*) 3.07×10^{-17} (+) 8.27×10^{-18} (+,†) 2.31×10^{-17} (+) 9.66×10^{-18} (+,†) 5.83×10^{-17} (+)
Gas entry-value (drying) (MPa)	0.3 (estimated)	S_r=0.97; 0.093 (PT[1]) S_r=0.95; 0.157 (PT[1]) S_r=0.93; 0.189 (PT[1]) S_r=0.90; 0.276 (PT[1])
Gas breakthrough pressure (MPa)	-	0.13-0.15 (*) 0.18-0.22 (+) 0.18-0.19 (+,†)

PT: small-scale point test (oedometer cell); IC : infiltration column (back-analysis); (1) Point test PT from [5, 6, 10] GMT S/B at 1.8 Mg/m^3; (*) 1st MU-B test; (+) 2nd MU-B test; (++) test after gas flow; (†) test with a re-saturation stage of the previous breakthrough event

The authors acknowledge the financial support of 'National Cooperative for the Disposal of Radioactive Waste' Nagra (Switzerland) through a competitive research project (GAST – Laboratory investigation of two-phase transport in sand-bentonite mixtures, ref 18311, 2019-2022) with the 'International Centre for Numerical Methods in Engineering' CIMNE (Spain). Furthermore, the authors acknowledge the fruitful discussions with Prof. Eduardo Alonso, Prof. Sebastia Olivella, Dr Juliana Knobelsdorf, Dr Laura Gonzalez-Blanco, Dr Nuria Pinyol, Dr Bill Lanyon, Dr Thomas Spillmann, Dr Andreas Reinicke, and the technical design/construction of the two mock-up prototypes by MSc Mercedes Sondon. The help of Dr Arisleidy Mesa-Alcantara, MSc Luis Miguel Garcia and MSc Cesarina Quezada in the laboratory tests is greatly acknowledged.

References

1. N. Khalili, E. Romero & FA Marinho, *State of the Art Report. Advances in unsaturated soil mechanics: Constitutive modelling, experimental investigation, and field instrumentation*, in Proceedings of the ICSMGE 2022, 1-5 May 2022, Sydney, Australia (2022)
2. National Cooperative for the Disposal of Radioactive Waste (Nagra), *Effects of post-disposal gas generation in a repository for low- and intermediate- level waste sited in the Opalinus Clay of Northern Switzerland.* Nagra Tech. Report NTB 08-07, Wettingen, Switzerland (2008)
3. J. Rüedi, S. Teodori, T. Spillmann, M. Reinhold, T. Trick, M. Keller, et. al. *Gas-Permeable Seal Test at GTS: As-Built Report.* Nagra Tech. Report NAB 12-59, Wettingen, Switzerland (2012)
4. *GAST - Gas-Permeable Seal Test*, GTS Grimsel Test Site. Retrieved April 2023, from https://www.grimsel.com/gts-projects/gast/gast-introduction
5. E. Romero, E.E. Alonso, J. Knobelsdorf, *Laboratory tests on compacted sand/bentonite buffer material for the GMT emplacement project.* Nagra Tech. Report GMT/IR 01-06, Wettingen, Switzerland (2002)
6. E. Romero, I. García, E.E. Alonso, *Laboratory gas tests on compacted sand-bentonite buffer material used in the GMT in-situ emplacement.* Nagra Tech. Report GMT/IR 02-02, Wettingen, Switzerland (2003)
7. E. Romero, C. Alvarado, M. Sondon, A. Lloret, E. E. Alonso, A. Reinicke, *Mini-GAST Mock-ups to support GAST (gas-permeable seal test). Commissioning and first water and gas transport results*, in 8th International Conference on Clays in Natural and Engineered Barriers for Radioactive Waste Confinement, 13-16 June 2022, Nancy, France (2022)
8. A. Seiphoori, *Thermo-hydro-mechanical characterisation and modelling of Wyoming granular bentonite*, Technical Report NAB 15-05, EPFL, Lausanne (2015)
9. D. Manca, *Hydro-chemo-mechanical characterisation of sand/bentonite mixtures, with a focus on the water and gas transport properties,* Ph.D. thesis, EPFL, Lausanne (2015)
10. E. Romero, Eng. Geo. **65**, 3 (2013)
11. T. Hokari, M. Okihara, T. Ishii, T. Ishii, H. Ikuse, MRS Proc. **465**, 1019 (1996)
12. S. Olivella, J. Vaunat, A. Rodriguez-Dono. CODE_BRIGHT 2022 User's Guide (2022). https://deca.upc.edu/en/projects/code_bright
13. E. E. Alonso, A. Gens, A. Josa, Géotech. **40**, 3, 405 (1990)